A&A 594, A121 (2016)
DOI: 10.1051/0004-6361/201527959

Astronomy & Astrophysics

The Bullet cluster at its best: weighing stars, gas, and dark matter

D. Paraficz[1,2], J.-P. Kneib[1], J. Richard[3], A. Morandi[4], M. Limousin[2], E. Jullo[2], and J. Martinez[3]

[1] Laboratoire d'Astrophysique École Polytechnique Fédérale de Lausanne (EPFL), Observatoire de Sauverny 1290 Versoix, Switzerland
e-mail: danuta.paraficz@epfl.ch
[2] Aix-Marseille Université, CNRS, LAM (Laboratoire d'Astrophysique de Marseille), UMR 7326, 13388 Marseille, France
[3] Univ. Lyon1, ENS de Lyon, CNRS, Centre de Recherche Astrophysique de Lyon, UMR 5574, 69230 Saint-Genis-Laval, France
[4] Physics Department, University of Alabama in Huntsville, Huntsville, AL 35899, USA

Received 14 December 2015 / Accepted 11 August 2016

ABSTRACT

Aims. We present a new strong lensing mass reconstruction of the Bullet cluster (1E 0657-56) at $z = 0.296$, based on WFC3 and ACS HST imaging and VLT/FORS2 spectroscopy. The strong lensing constraints underwent substantial revision compared to previously published analysis, there are now 14 (six new and eight previously known) multiply-imaged systems, of which three have spectroscopically confirmed redshifts (including one newly measured from this work).
Methods. The reconstructed mass distribution explicitly included the combination of three mass components: (i) the intra-cluster gas mass derived from X-ray observation; (ii) the cluster galaxies modeled by their fundamental plane scaling relations and (iii) dark matter.
Results. The model that includes the intra-cluster gas is the one with the best Bayesian evidence. This model has a total rms value of 0.158″ between the predicted and measured image positions for the 14 multiple images considered. The proximity of the total rms to resolution of HST/WFC3 and ACS (0.07−0.15″ *FWHM*) demonstrates the excellent precision of our mass model. The derived mass model confirms the spatial offset between the X-ray gas and dark matter peaks. The fraction of the galaxy halos mass to total mass is found to be $f_s = 11 \pm 5\%$ for a total mass of $2.5 \pm 0.1 \times 10^{14}\ M_\odot$ within a 250 kpc radial aperture.

Key words. gravitational lensing: strong – galaxies: clusters: individual: Bullet cluster

1. Introduction

The massive galaxy cluster, 1E 0657-56, discovered by Tucker et al. (1998) consists of two colliding galaxy clusters at $z = 0.296$. In this distinct merging system, a sub-cluster, the "bullet" has collided with the main cluster, approximately in the plane of the sky (Barrena et al. 2002). The bullet-like sub-cluster has produced strong bow shock in the intra-cluster gas during the collision and consequently the collision stripped the gas from the cluster potential (Markevitch et al. 2002). The offset between the two baryonic components (gas and galaxies) gave a remarkable possibility for the indirect measurements of the total mass distribution using gravitational lensing studies (Mehlert et al. 2001; Clowe et al. 2004; Bradač et al. 2006, 2009), which unambiguously demonstrated that dark matter (DM) traces the collisionless galaxies and not the X-ray gas. The study of the lensing mass distribution of the Bullet cluster remains a powerful evidence of the DM existence that severely challenges theories of modified gravity such as MOND and TeVeS (Milgrom 1983; Bekenstein 2004). It also gives upper limits on the DM self interaction cross section (Randall et al. 2008; Markevitch et al. 2004) and lower limit on the possible radiative decay of DM (Boyarsky et al. 2008).

Since the first lensing mass measurement of the Bullet cluster considerable effort has been put in constraining its mass distribution. Nevertheless, significant discrepancies exist, for example, the masses at $R < 200$ kpc derived from the Clowe et al. (2004) and Bradač et al. (2006) differ by a factor of two. Although, this is likely due to degeneracies of lens modeling between strong and weak lensing mass estimates, the Bradač et al. (2006) mass measurement uncertainty is still as high as 14% over the full ACS field. Indeed, the complexity of the Bullet cluster and the limited number of multiple images makes its strong lens modeling exceptionally challenging.

As witnessed in other clusters (e.g., Abell 1689, 1703, 2218, see Richard et al. 2010b), the accuracy of the lensing mass map is strongly dependent on the correct identification and on the number of multiply-imaged systems used to constrain it. This accuracy has a further impact on the measurements of magnification of high redshift galaxies (Bradač et al. 2009; Hall et al. 2012) and the luminosity function estimations. Hence, to construct a robust mass model of an accurate gravitational telescope many spectroscopically confirmed multiply-imaged systems are needed. Therefore, The Bullet cluster does not compete with the Frontier Field clusters as gravitational telescope (Jauzac et al. 2015; Richard et al. 2014), nevertheless the methods developed in this work, could be implemented also to other galaxy clusters.

In this work we present an improved high-resolution strong lensing mass model of the Bullet cluster (the combination of weak lensing and our newly reconstructed strong lensing model will be published in our next paper) based on the identification of new multiply-imaged systems. These results are based on Advanced Camera for Surveys (ACS) and Wide Field Camera 3 (WFC3) new images as well as on new spectroscopic redshift

determination of multiply-imaged systems, one taken from the literature and one obtained through VLT/FORS2 observations. Furthermore, our mass reconstruction includes the novel combination of the following mass components: (i) the intra-cluster gas mass derived from X-ray observation; (ii) the cluster galaxies modeled by their fundamental plane scaling relations and (iii) dark matter. The gas mass component is distinctive in the Bullet cluster since the gas is spatially shifted from the main mass component of the cluster (~47″ Clowe et al. 2006) and has been thoroughly studied. Nevertheless, until now the X-ray data of a gas component of this cluster has not been independently taken into account in any of the lens modeling. Enriching our modeling technique and improving the lensing constraints allowed us to create a more accurate mass model with significantly smaller systematic uncertainties.

This paper is structured as follows. Section 2 describes the data and its reduction procedures. Section 3 describes the previous achievements in the field and presents our multiply-imaged systems. Section 4 presents the method of mass reconstruction of the Bullet cluster, describes newly implemented mass modeling improvements (new scaling relations and X-rays mass map). Our conclusions are summarized in Sect. 5.

Throughout the paper, we assume a Λ cold dark matter (ΛCDM) cosmology with $\Omega_m = 0.3$, $\Omega_\Lambda = 0.7$ and $h_{100} = 0.7$. At the cluster redshift $z = 0.296$, 1″ corresponds to 4.413 kpc.

The reference center of our analysis is fixed at the BCG 1 center: $\alpha = 104.6588589$ $\delta = -55.9571863$ (J2000.0). Magnitudes are given in the AB system. Unless stated otherwise, all uncertainties and upper and lower limits are given and/or plotted at 1σ confidence level.

2. Observations and data reduction

2.1. Hubble imaging

The first round of observation of the cluster 1E 0657-56 with the *Hubble* Space Telescope (HST) was carried out between 2004 and 2006 using the ACS camera (HST programs 10200 and 10863, PI: Jones & Gonzalez) at two side-by-side positions covering the main cluster and the Western sub-cluster. The main cluster was observed in *F606W*, *F775W* and *F850LP* bands (hereafter V, i, z), and the sub-cluster in *F435W*, *F606W*, *F814W* (hereafter B, V, I; see Figs. 1 and 2). The *F606W* band covering both components is used for a uniform view of the cluster, as well as detections in the photometric catalog. Details on the exposure times and quality of these data have been presented in Bradač et al. (2009).

In addition, HST/WFC3 imaging has been performed in *F110W* and *F160W* bands, with two largely overlapping positions centered on the main cluster (PID: 11099; PI: Bradač), and with a single pointing at the center of the main cluster (PID:11591; PI: Kneib). The total exposure time in *F110W*/*F160W* was 6529/7029 s for the first program, and 3211/2811 s for the second program, with 9740/9840 s in the overlapping region. The magnitude limits at $3-\sigma$ measured using 0.25″ radius aperture the deepest data reach 28.76 and 28.15 in *F110W* and *F160W* band, respectively.

Finally, in February 2011, the main cluster of 1E 0657-56 was observed with the ACS camera using the *F814W* filter as part of the program 11591. The total exposure time was 4480 s (2 orbits).

Both ACS and WFC3 data have been aligned using the multidrizzle (Koekemoer et al. 2002) software, including some relative shifts measured with IRAF[1] for datasets taken at different epochs. The *F606W* image was used for overall alignment of the different bands, and the USNO B1.0 catalog provided absolute astrometric calibration.

We use the double-image mode (with *F606W* being a detection image) of the SExtractor package (Bertin & Arnouts 1996) to detect objects and compute magnitudes within a 0.5″ diameter aperture (ACS images). All of our imaging data (optical/ACS and near-IR/WFC3) are PSF-matched to the WFC3/IR *F160W* imaging data before making color measurements. We measure isophotal magnitudes to produce accurate colors and photometric redshifts.

The half-light radius $R_{\rm eff}$ used in the fundamental plane galaxy scaling was measured using the Galapagos on *F606W* image.

2.2. Cluster member identification

Cluster galaxies were identified based on the ACS data using the characteristic cluster red-sequences identified using the $[(V-I)$ vs. $V]$ or $[(V-z)$ vs. $V]$ color−magnitude diagrams (see Fig. 3), for the main and sub-cluster components, respectively. The galaxies lying in one of the red sequences were assumed to be cluster members. In order to save computing time we have included in the lens modeling only the 100 brightest cluster galaxies ($V < 25.2$), that roughly corresponds to lensing deflection larger than ~0.1″).

2.3. VLT/FORS2 spectroscopy

We have used the FOcal Reducer and low dispersion Spectrograph (FORS2, Appenzeller et al. 1998) at the Very Large Telescope to measure the spectroscopic redshift of multiply-imaged systems. MXU masks with 1″-wide slits were designed to cover most of the multiple images identified in the Bullet cluster. Observations were obtained on the 3 nights of February 15−17th 2010, with a total of 9.9 ks split into 900 s exposures. The G300V grism and the GG435 order-sorting filter were used to provide a good coverage of the reddest wavelengths ($4450 < \lambda < 8650$ Å) a dispersion of 2.69 Å per pixel and a resolution $R = \lambda/\Delta\lambda \sim 200$ at the central wavelength 5900 Å. Standard stars were observed during the same nights, and the data reduction was performed with a combination of the esorex package and standard IRAF routines to improve the sky subtraction and wavelength calibration of specific slits.

Within these shallow spectroscopic data we only manage to measure the redshift for two systems. We confirm the $z = 3.24$ spectroscopic redshift of system A, previously found by Mehlert et al. (2001). We also measured the redshift of system H, one of the multiply-imaged systems identified in the sub-cluster. This source shows a strong emission line at 4851 Å which we interpret as Lyman-α at $z = 2.99$ from the lensing configuration and the lack of additional emission lines. The other likely alternative is [OII], observed at 4851 Å would give a redshift of 0.301, similar to the cluster redshift, thus the alternative can be excluded (see Fig. 4).

[1] IRAF is distributed by the National Optical Astronomy Observatory, which is operated by the Association of Universities for Research in Astronomy (AURA) under cooperative agreement with the National Science Foundation.

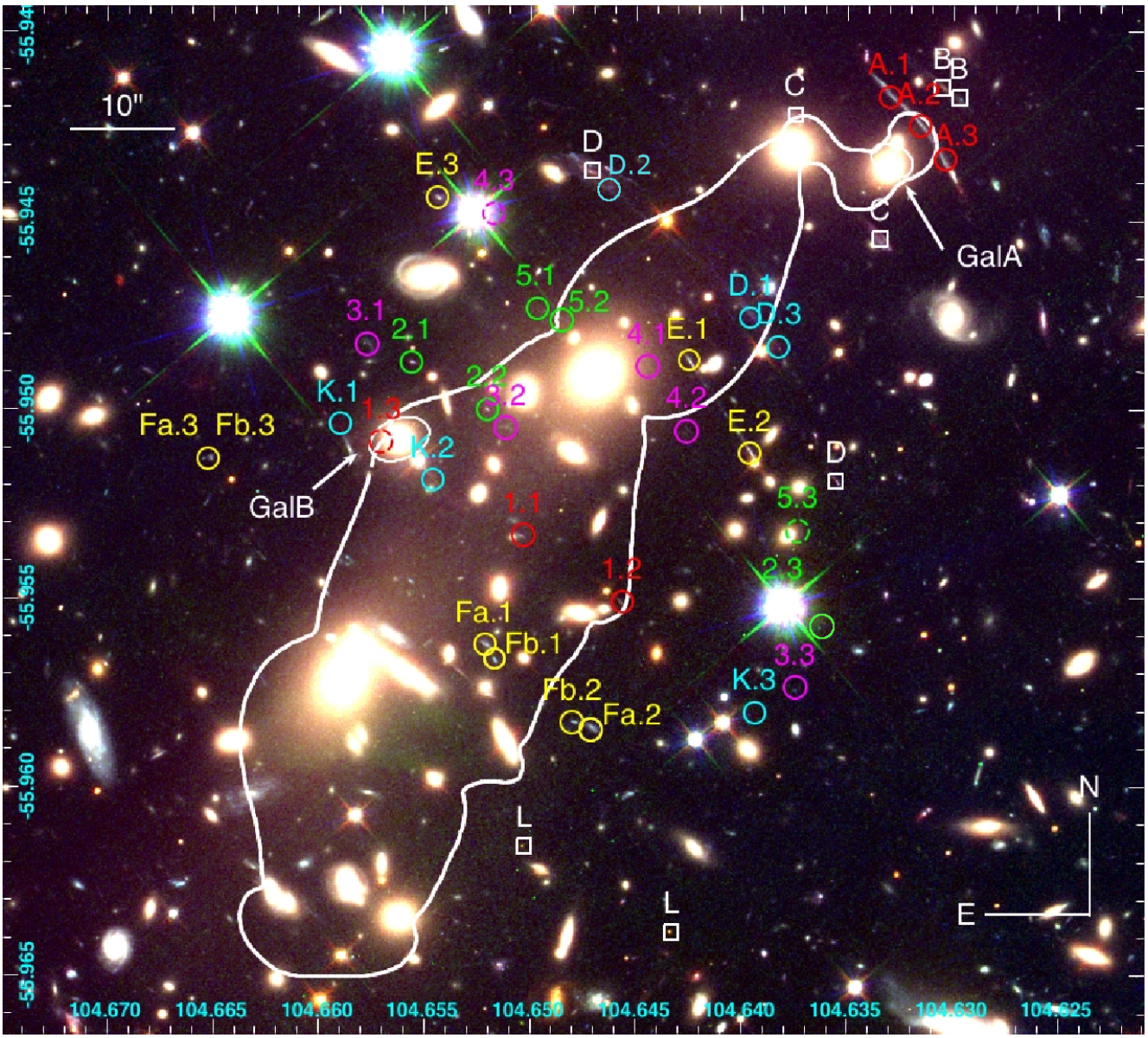

Fig. 1. Color HST image of the main cluster component of 1E 0657-56 (blue–*F606W*, green–*F814W*, red–*F160W*). Multiple images considered in this work are marked with color circles (dashed line circles mark the predicted but not confirmed positions of counter images), the spectroscopically confirmed multiply-imaged systems are system A (Mehlert et al. 2001) and K (Gonzalez et al. 2010). White squares are referring to Bradač et al. (2009) systems, which we have revised and we did not include in our modeling. The new identification of system A is shown in red and the new identification of system D is shown in cyan (see also Fig. 7). System D is a multiply-imaged candidate and due to extended morphology is not a part of model constraints. The white line represents a critical line corresponding to $z = 3.24$.

3. Multiple-image identification

3.1. Previous work

The first lens model of the Bullet cluster, derived by Mehlert et al. (2001) was based on 3 modeled DM clumps as SIS and SIE and 150 cluster members modeled using the Faber-Jackson relation (Faber & Jackson 1976). As lensing constraints Mehlert et al. (2001) used 6 multiply-imaged systems (labeled A to F selected from deep BgRI VLT/FORS images). For one of the multiple systems (the giant arc) they measured a spectroscopic redshift of $z = 3.24$.

Bradač et al. (2006, 2009) applied a grid based mass reconstruction method based on strong and weak gravitational lensing (their weak lensing signal was taken from Clowe et al. 2004, 2006). Using deep, high-resolution optical data from 3 ACS bands (*F435W*, *F606W*, and *F814W*), *BVR* data from Magellan and *I*-band from VLT/FORS (Clowe et al. 2004) they confirmed (based on photometry and morphology) six multiply-imaged systems as discovered by Mehlert et al. (2001; labeled A–F) and also identified 4 new additional systems (G–J) in the sub-cluster region, where none were previously known. The combined mass reconstruction of Bradač et al. (2006) provided a high-resolution, absolutely calibrated mass map, with a projected, enclosed mass $M_{>250\ \mathrm{kpc}} = 2.8 \pm 0.2 \times 10^{14}\ M_{\odot}$ around the main cluster and $M_{>250\ \mathrm{kpc}} = 2.3 \pm 0.2 \times 10^{14}\ M_{\odot}$ around the sub-cluster.

3.2. Critical evaluation of previously identified systems and new identification

We have reviewed each strongly lensed candidate proposed by Mehlert et al. (2001), Bradač et al. (2006, 2009) by checking

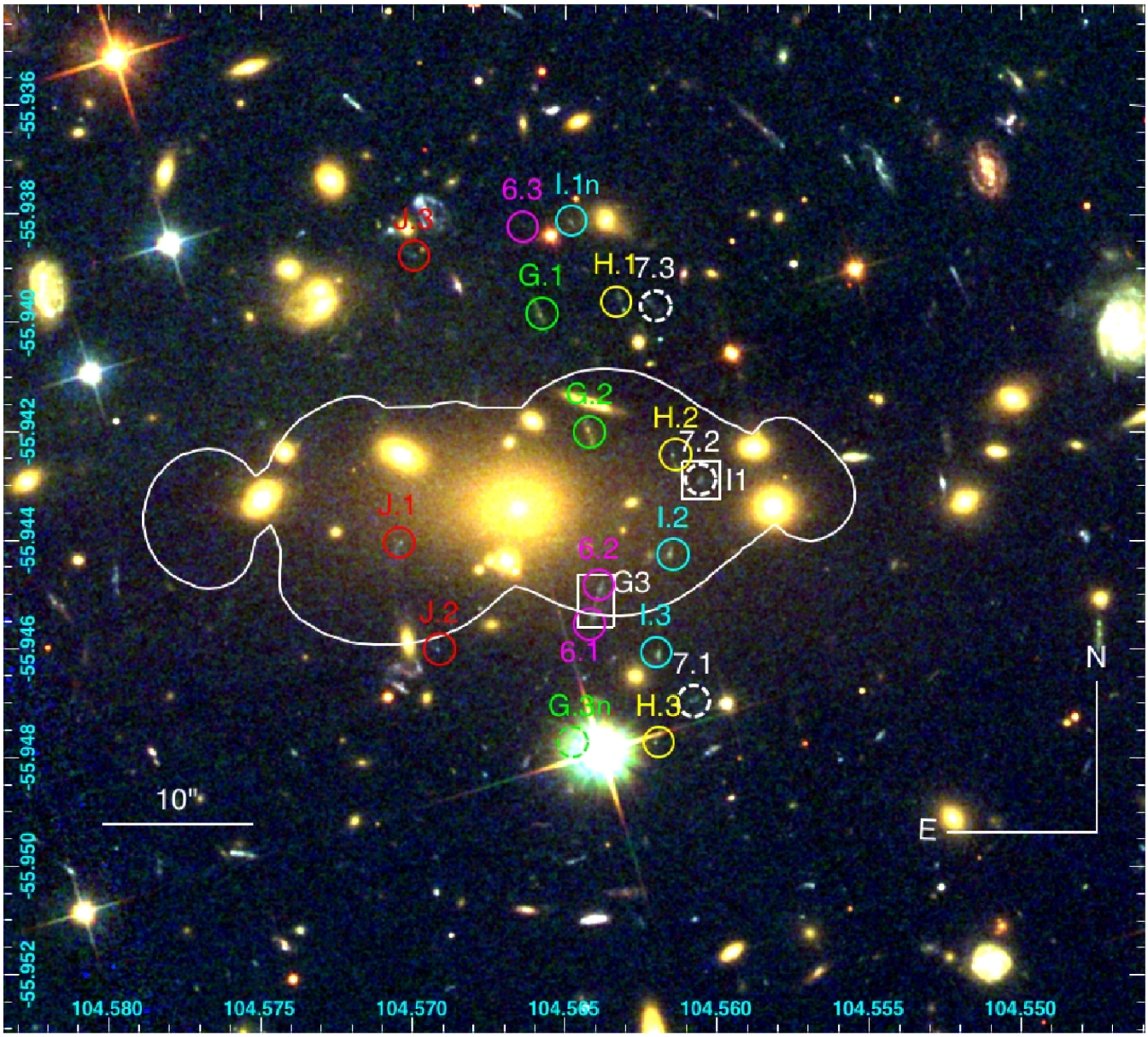

Fig. 2. Color ACS/HST image of the sub cluster component of 1E 0657-56 (blue–*F435W*, green–*F606W*, red–*F814W*). Multiple images considered in this work are marked with color circles (dashed line circles mark the predicted but not confirmed positions of counter images). In this work, we spectroscopically measured a redshift of $z = 2.99$ for the multiply-imaged system H (see Sect. 2.3). System 7 (white dashed circle) is a multiply-imaged candidate and is not a part of model constraints due to large color uncertainties. The white line represents the critical line at redshift $z = 2.99$.

(1) the morphology (2) color agreement and (3) the consistency with the lensing mass model prediction. In the end, we have only used those systems that have passed all three tests. By color agreement, we call images that "color distance" is less than 5.5. "Color distance" is defined as

$$\left[\sum_{ij} \mid c_i - c_j \mid / \sqrt{cerr_i^2 + cerr_j^2}\right] /N, \quad (1)$$

where c_i, c_j are colors and $cerr_i, cerr_j$ are color errors.

In order to avoid confusion between our and previous multiple image identification, we choose to keep alphabetical notation (A−L), for only those multiple image systems that were already reported by Bradač et al. (2006, 2009), while for our newly identified images we use numerical notation (1−7). Altogether, our set of constraints is quite different from the one of Bradač et al. (2009). Indeed, we have rejected 3 multiple-image systems (B, C and L) and changed system A, D and E, for the following reasons:

– system A: Bradač et al. (2006) matched two symmetric images A1 and A2 forming a giant arc, whereas the expected third image A3 is not detected. Moreover, the analysis of *Spitzer*/MIPS and *Herschel* data of the Bullet cluster performed by Rex et al. (2010) shows that only A1 is detected in the Far-IR (source HLS12 from this paper) and therefore the identification of the system is incorrect (see Table 2). To reconciliate the identification with the far-infrared observations, we interpret the giant arc as the merging of 3 images crossing the critical line at $z = 3.24$ (system A.1, A.2 and A.3 in our notation; see Fig. 5 and Table 4);

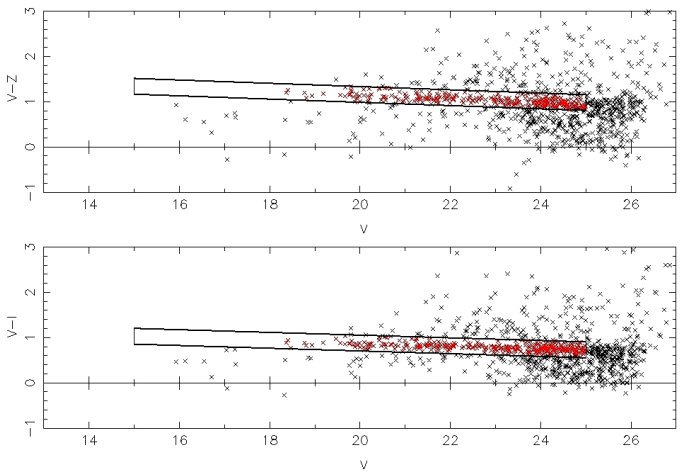

Fig. 3. Color−magnitude diagrams and the selection of cluster member galaxies. The red sequence selection is shown in the black boxes: all galaxies in this box are considered to be cluster galaxies. [$(V - I)$ vs. V] or [$(V - z)$ vs. V] color−magnitude diagrams correspond to the main and sub-cluster components, respectively.

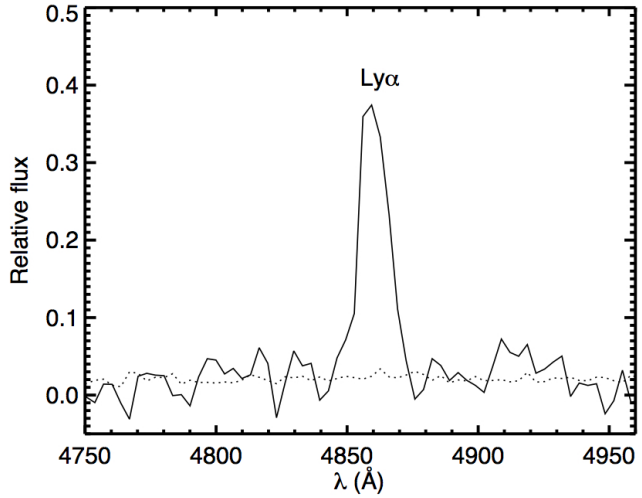

Fig. 4. System H shows a strong emission line at 4851 Å which we interpret as Lyman-α at $z = 2.99$ from the lensing configuration and the lack of additional emission lines. The dotted line is the sky noise spectrum (no sky emission line are present in this wavelength range). The other likely alternative is [OII], observed at 4851 Å would give a redshift of 0.301, similar to the cluster redshift, thus the alternative can be excluded.

- system B: according to our model (which now takes into account triply-imaged system A) B is a single imaged arc, also the colors between B1 and B2 used by Bradač et al. (2006) are clearly different as seen in Fig. 5 and Table 3;
- system C: the predicted third image is not detected (see also Table 3);
- system D: is problematic due to extended morphology and the large uncertainty in locating the different multiple image centers, thus we do not add it to the set of the systems that constrain the mass model, instead we use the mass model to predict two new image positions D.1 and D.3 and their redshift (see Table 4, Figs. 1 and 7);
- system E: (in our notation system 3), we find its third counter image E.3;
- system L: the two images L1 and L2 reported by Bradač et al. (2009) have slightly color inconsistency (L1 is brighter than L2 by ∼0.5 mag in all the filters except for *F606W* filter where L2 is detected with >5σ and L1 is not detected with <1.5σ), "color distance" is 3.6, additionally, positions of multiple images is entirely excluded by the geometry of our model (rms > 10″).

Table 1. Photometry of the components of the multiply-imaged system I.

Name	*F606W*	*F435W* – *F606W*	*F606W* – *F814W*
I.1[a]	26.49 ± 0.11	0.18 ± 0.18	−0.22 ± 0.15
I.1n[b]	26.36 ± 0.14	0.47 ± 0.11	0.17 ± 0.07
I.2	25.55 ± 0.07	0.50 ± 0.07	0.08 ± 0.04
I.3	25.60 ± 0.05	0.49 ± 0.06	0.03 ± 0.04

Notes. We note the strong color difference in *F606W* – *F814W* colors for the old I.1[(a)] by Bradač et al. (2006) and new, this paper I.1n [(b)] identification. See also Figs. 2 and 6.

In the sub-cluster, we have also excluded/added the following images of the I, J and G systems:

- old image I1, identified by Bradač et al. (2009) has a significantly different color than images I2 and I3, instead we have found an object "new I1n" that better fits the position and color of the system (see Table 1 and Fig. 2);
- according to the geometry of our mass model, the old G3 identification can not belong to the same system as images G1 and G2. The model predicts position of the third counterpart G3 of the system directly on the bright star, south of the cluster. We displayed the new G3n position predicted by the model in Fig. 2;
- we believe that the old G3 is a "straight" arc made of 2 merging images (named "6.1" and "6.2" in our notation, see Fig. 2) with an identified third counterpart in the North part of the sub-cluster (6.3);
- we identified the third image of the system J (J.3 as shown in Fig. 2).

The three remaining multiply-imaged systems from Bradač et al. (2009) F and K in the main cluster and H in the sub-cluster, were included in our set of constraints without changes.

Finally, thanks to the new deep WFC3 and ACS images, we have identified 6 new secure multiply-imaged systems, five new systems (1−5) in the main cluster and one new system (6) in the sub-cluster. We have also identified system 7 in the sub-cluster, however due to large uncertainties in the color of this system, we do not use it as a part of our model constraints, instead we present it only as a possible multiply-imaged candidate.

In Figs. 5−7 we show postage stamps of all multiple images (except for system K that is not visible in HST/ACS and barely detected in HST/WFC3, see Bradač et al. 2009 for a *Spitzer* postage stamps), their exact locations, photometry, magnitudes, colors, magnifications and redshifts are given in Table 4.

In total, we use 14 strongly lensed systems (9 systems in the main cluster region and 5 systems in the sub-cluster region), three of those systems (A, K and H) have measured spectroscopic redshifts. System A is the bright giant arc with previously measured spectroscopic redshift at $z = 3.24$ by Mehlert et al. (2001; see Fig. 5), system K is an IRAC bright submm source, dusty galaxy, with well measured redshift $z = 2.79$ by Gonzalez et al. (2010), and system H at redshift $z = 2.99$ was measured in this paper with FORS/VLT (see Sect. 2.3).

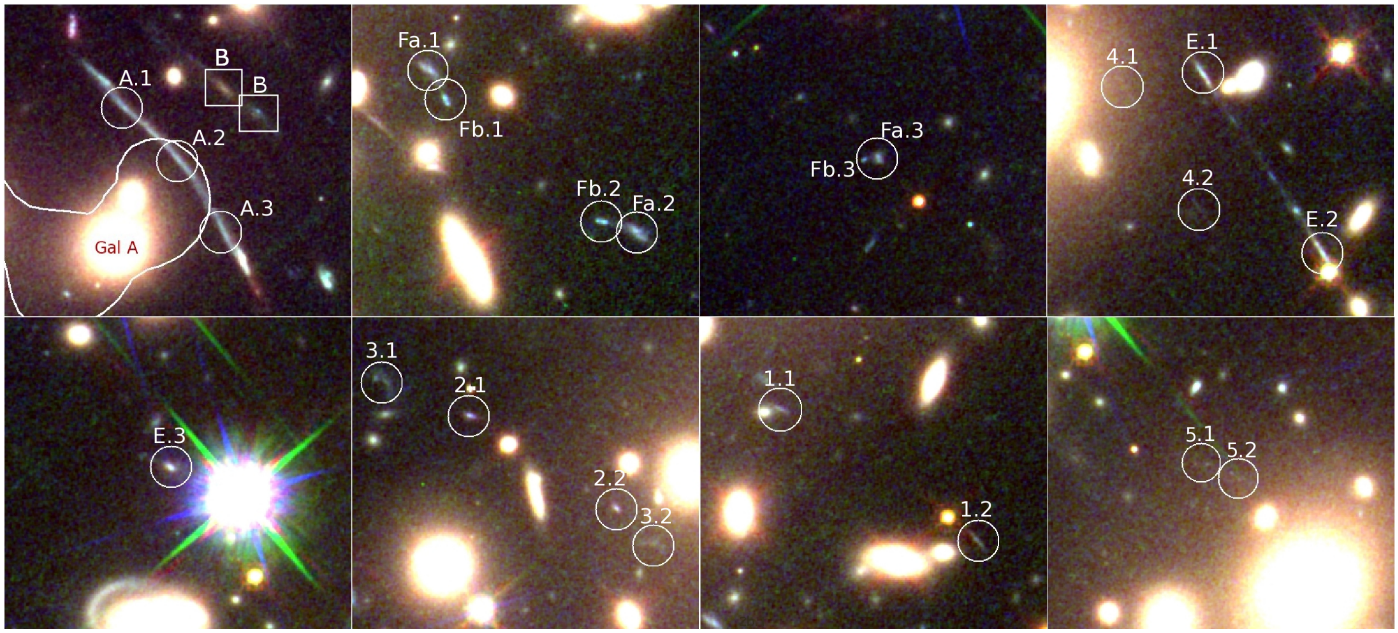

Fig. 5. Multiple images identified in the main cluster area with the HST images, as shown in Fig. 1. System K is not shown since it is invisible in ACS/HST. The size of each box is 12″ × 12″, North is up and East is left.

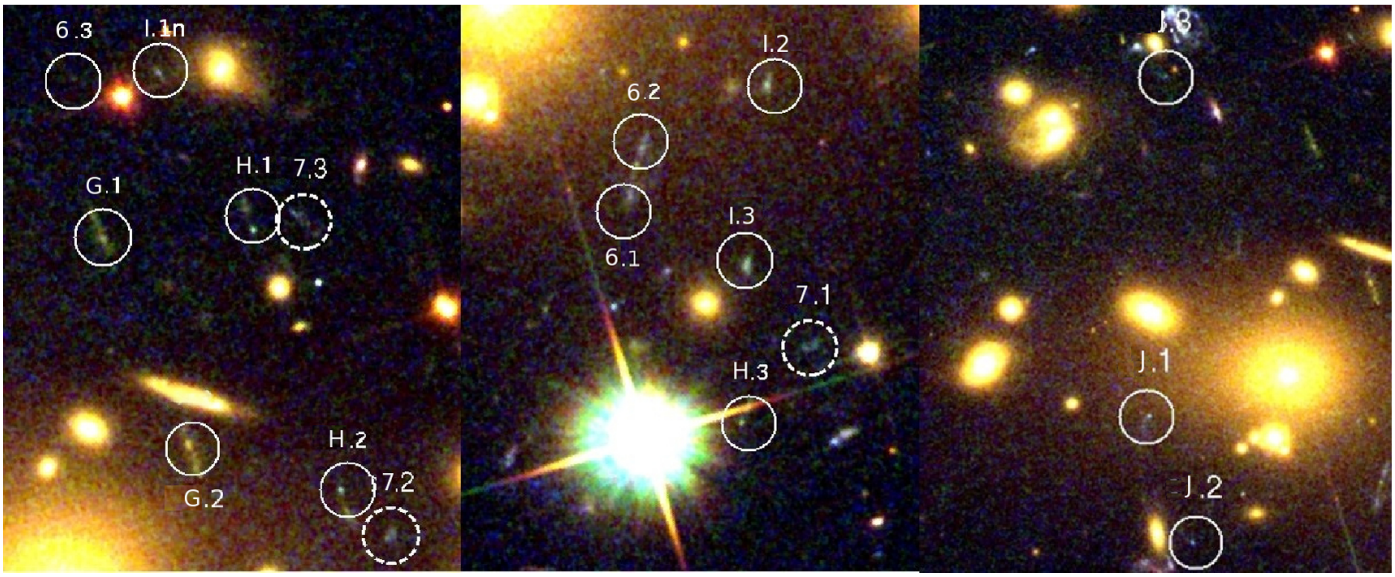

Fig. 6. Multiple images identified in the sub cluster area with the ACS images, as shown in Fig. 2. Multiple images marked with dashed line circles mark the predicted but not confirmed positions of counter images. System 7 with dashed circle, is a multiply-imaged candidate and is not a part of model constraints due to large color uncertainties. The size of each box is 20″ × 12″, North is up and East is left.

Table 2. Photometry of the components of the multiply-imaged system A as identified by Bradač et al. (2009).

	RA	Dec	*F606W*	MIPS	*F606W – F775W*	*F775W – F850LP*	*F850LP – F110W*	*F110W – F160W*
A	104.63332	–55.941377	25.71 ± 0.04	0.06 mJy	0.39 ± 0.03	0.10 ± 0.02	0.11 ± 0.02	0.22 ± 0.01
A	104.63020	–55.943620	25.00 ± 0.04	<0.016 mJy	0.86 ± 0.03	0.04 ± 0.01	0.01 ± 0.01	0.33 ± 0.01

Notes. We note the strong color difference between MIPS and other filters OF the old A system identification by Bradač et al. (2006) and good color agreement of new system A identification (see Table 4). See also Figs. 1 and 5.

4. Lensing methodology

4.1. Overview

The strong-lensing mass reconstruction is based on the Bayesian Monte Carlo Markov chain (MCMC) method implemented in the LENSTOOL[2] software (Kneib et al. 1996; Jullo et al. 2007; Jullo & Kneib 2009).

The mass distribution of the Bullet cluster is considered here as a superposition of three cluster-scale dark matter clumps

[2] See http://projets.oamp.fr/projects/lenstool/wiki

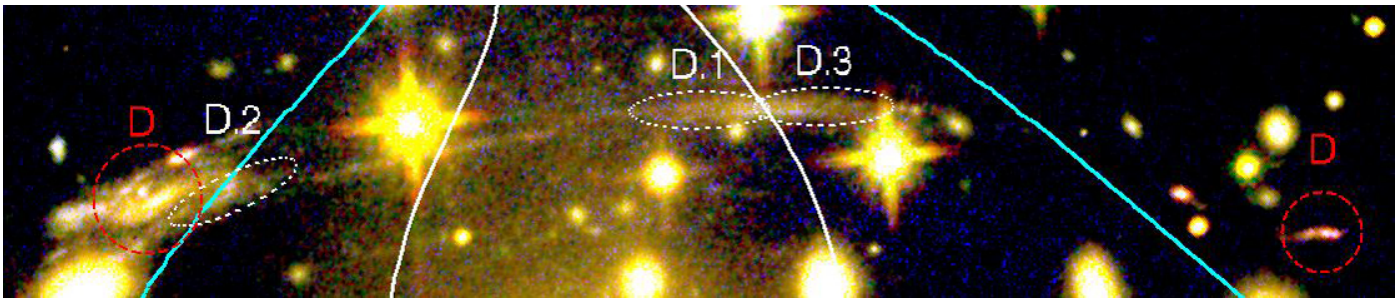

Fig. 7. Multiply-imaged system D, a giant arc, identified in the cluster area with the ACS images, as shown in Fig. 1. Multiple images marked with red dashed line circles mark the positions of images of system D as reported by Bradač et al. (2006). White ellipses mark the positions of multiple images of the D system predicted by our strong lensing mass model. The white line is the critical line at the model redshift corresponding to this candidate system ($z = 3.23$). Cyan lines mark limits of multiple image occurrence as predicted by our model.

Table 3. Photometry of the rejected systems B, C, D and L as identified by Bradač et al. (2009).

	RA	Dec	*F606W – F775W*	*F775W – F850LP*	*F850LP – F110W*	*F110W – F160W*
B	104.62968	–55.9418082	0.58 ± 0.09	0.05 ± 0.07	−0.01 ± 0.05	0.00 ± 0.03
B	104.63047	–55.9414692	0.90 ± 0.12	0.30 ± 0.07	0.36 ± 0.04	0.20 ± 0.01
C	104.63729	–55.942493	0.67 ± 0.23	0.32 ± 0.16	0.56 ± 0.11	0.36 ± 0.06
C	104.63339	–55.945603	0.23 ± 0.05	0.10 ± 0.06	0.49 ± 0.04	0.43 ± 0.02
L	104.64339	–55.963841	<2.93	0.43 ± 0.12	0.69 ± 0.08	0.28 ± 0.04
L	104.650356	–55.961562	1.35 ± 0.59	0.79 ± 0.21	0.77 ± 0.12	0.27 ± 0.05
D	104.64713	–55.943712	−0.25 ± 0.10	0.63 ± 0.08	0.32 ± 0.04	0.18 ± 0.02
D	104.63546	–55.951920	−0.75 ± 0.17	0.17 ± 0.22	0.39 ± 0.13	0.96 ± 0.02

(two in the main cluster and one in the sub-cluster), the BCGs, the intracluster gas and the individual galaxies.

The light distribution of the main cluster indicates cluster-scale dark matter bimodality. Nonetheless, we have checked the alternative possibility of main cluster consisting of only one dark matter clump. This alternative can not reproduce the position of the multiple images with as high precision as the two-clump model. It gives a significantly worse fit to the data (rms = 1.5″ vs. rms = 0.2″), confirming the existence for two large scale dark matter halos in the main clump. Therefore, the dark matter clumps are called DM1 and DM2 in the bimodal main clump and DM3 in the sub-clump.

All dark matter clumps and galaxies were parameterized as dual Pseudo Isothermal Elliptical mass distributions dPIE (Limousin et al. 2005). The dPIE is described by seven parameters: redshift, central position (x_c, y_c), ellipticity $\epsilon = \frac{a^2-b^2}{a^2+b^2}$ (with a and b being semi-major and semi-minor axis, respectively), the position angle θ, a core radius $r_{\rm core}$, a truncation radius $r_{\rm cut}$ and a fiducial velocity dispersion σ. The two scale radii, $r_{\rm core}$ and $r_{\rm cut}$, define changes in the slope of the dPIE density profile:

$$\rho(r) = \frac{\rho_0}{(1 + r^2/r_{\rm core}^2)(1 + r^2/r_{\rm cut}^2)}, \quad (2)$$

where ρ_0 is a central density. The profile is flat in the inner region, then isothermal ($\rho \sim r^{-2}$) between $r_{\rm core}$ and $r_{\rm cut}$, and steeply decreasing ($\rho \sim r^{-4}$) beyond $r_{\rm cut}$. Thanks to its extra degree of freedom compared to a NFW potential, the dPIE potential is more flexible in modeling complex galaxy clusters, such as 1E 0657-56. Moreover, the dPIE profile is specially suitable to model galaxies. Indeed, several studies, based on dynamics of stars, globular clusters and X-ray halos have shown that early-type galaxies are isothermal in their inner parts (Koopmans et al. 2006; Oguri 2007; Gerhard et al. 2001; Peng et al. 2004), with no significant evolution with redshift up to $z \sim 1$, this is also true for cluster members (see Natarajan et al. 1998, 2009). The dPIE has been successfully used to model galaxy clusters (e.g., Kneib et al. 1996; Richard et al. 2007), as well as early-type galaxies (e.g., Natarajan et al. 1998; Limousin et al. 2007a)

In the optimization procedure the dPIE parameters of cluster scale DM halos (the central position, ellipticity, velocity dispersion, core radius and the position angle) were allowed to vary freely. In case of the cluster galaxies, the position, ellipticity, and orientation were matched to that of the light distribution as measured by SExtractor. The velocity dispersions, core and cut-off radii of cluster members were scaled with their luminosity using common scaling relations (see Sect. 4.2).

BCGs and the 2 cluster galaxies (see Fig. 8) that are in the vicinity of multiple images were fitted individually, the same approach was used in lens modeling by Suyu & Halkola (2010), Limousin et al. (2008, 2007b), Richard et al. (2010b,a). Firstly, because both BCG and galaxies that are in the vicinity of multiple images have strong influence on the multiple images position. Secondly, because BCGs are likely distinct galaxy population from cluster ellipticals, hence they do not follow common scaling laws (Natarajan et al. 1998). The two galaxies that are used explicitly in the optimization procedure are: galaxy A (104.63308, −55.943594) which strongly affects the brightest tangential arc (system A) and galaxy B (104.65626, −55.950795) which affects the multiply-imaged systems 1 and K (see Figs. 1 and 5).

The baryonic matter content of galaxy clusters is dominated by the X-ray emitting intra-cluster gas, the mass of which reaches 10−15% (David et al. 1993; Neumann & Arnaud 2001; Vikhlinin et al. 2006; LaRoque et al. 2006) of the total mass. As the emissivity of the X-ray emitting gas is proportional to the square of its density, the gas mass profile in a cluster can be precisely determined from X-ray data. In the case of the Bullet cluster there is a significant offset between the gas and

Table 4. Multiply-imaged systems used to constrain the model, with their ID, centroid position, brightness, colors, linear magnification and predicted or spectroscopically measured redshifts.

System	RA (deg)	Dec (deg)	*F606W*	*F606W – F775W*	*F775W – F850LP*	*F850LP – F110W*	*F110W – F160W*	μ	$z_{\rm phot}$	$z_{\rm m}^{a}$	$z_{\rm spec}$
Main Clump											
A.1	104.63293	–55.941725	25.59 ± 0.07	0.64 ± 0.09	0.02 ± 0.09	0.13 ± 0.08	0.41 ± 0.05	29.56 ± 8.97	$3.98^{+0.04}_{-0.07}$	–	3.24
A.2	104.63158	–55.942454	25.65 ± 0.05	0.51 ± 0.09	0.09 ± 0.09	0.21 ± 0.07	0.42 ± 0.04	26.22 ± 6.68	$3.09^{+0.45}_{-0.62}$	–	–
A.3	104.63055	–55.943405	25.67 ± 0.06	0.66 ± 0.11	0.02 ± 0.09	0.02 ± 0.08	0.37 ± 0.06	12.48 ± 0.90	$3.17^{+0.03}_{-0.14}$	–	–
Fa.1[b]	104.65210	–55.956245	24.63 ± 0.06	0.30 ± 0.08	−0.07 ± 0.09	0.15 ± 0.08	0.42 ± 0.05	9.77 ± 0.44	$2.86^{+0.35}_{-0.25}$	2.14 ± 0.19	–
Fa.2	104.64704	–55.958497	24.12 ± 0.05	0.22 ± 0.03	−0.08 ± 0.03	0.18 ± 0.03	0.41 ± 0.05	11.11 ± 0.72	$2.70^{+0.61}_{-0.24}$	–	–
Fa.3	104.66515	–55.951289	25.33 ± 0.11	0.37 ± 0.15	−0.01 ± 0.15	0.08 ± 0.14	0.52 ± 0.09	4.89 ± 0.22	$2.96^{+0.20}_{-0.27}$	–	–
Fb.1[b]	104.65165	–55.956641	25.31 ± 0.09	0.30 ± 0.08	−0.07 ± 0.09	0.14 ± 0.08	0.39 ± 0.08	14.91 ± 1.11	$3.10^{+0.54}_{-0.93}$	–	–
Fb.2	104.64786	–55.958292	25.09 ± 0.12	0.24 ± 0.04	−0.03 ± 0.04	0.06 ± 0.04	0.13 ± 0.10	15.02 ± 0.96	$2.85^{+0.35}_{-0.19}$	–	–
Fb.3	104.66544	–55.951301	26.61 ± 0.36	0.45 ± 0.11	−0.08 ± 0.11	0.04 ± 0.10	0.27 ± 0.09	4.77 ± 0.21	$3.98^{+0.40}_{-1.62}$	–	–
E.1	104.64242	–55.948720	25.52 ± 0.05	0.49 ± 0.08	0.11 ± 0.07	0.15 ± 0.06	0.43 ± 0.08	15.96 ± 1.36	$3.50^{+0.38}_{-0.45}$	3.17 ± 0.27	–
E.2	104.63954	–55.951165	25.51 ± 0.04	0.55 ± 0.08	0.22 ± 0.06	0.11 ± 0.05	0.37 ± 0.05	16.72 ± 1.30	$3.16^{+0.39}_{-0.50}$	–	–
E.3	104.65434	–55.944392	25.77 ± 0.04	0.45 ± 0.07	0.33 ± 0.06	0.20 ± 0.05	0.42 ± 0.06	7.13 ± 0.40	$2.96^{+0.01}_{-0.02}$	–	–
K.1	104.65864	–55.950557	–	–	–	–	–	–	–	–	2.79
K.2	104.65459	–55.951876	–	–	–	–	–	–	–	–	–
K.3	104.63929	–55.958032	–	–	–	–	–	–	–	–	–
1.1	104.65049	–55.953339	27.20 ± 0.13	0.25 ± 0.17	0.19 ± 0.25	0.89 ± 0.18	0.17 ± 0.04	15.65 ± 1.20	$2.03^{+0.96}_{-0.54}$	1.21 ± 0.23	–
1.2	104.64572	–55.955109	26.83 ± 0.11	0.29 ± 0.09	0.30 ± 0.07	0.50 ± 0.05	0.24 ± 0.05	11.20 ± 0.57	$1.39^{+1.07}_{-0.39}$	–	–
1.3*	104.65706	–55.950866	–	–	–	–	–	–	–	–	
2.1	104.65560	–55.948760	25.62 ± 0.06	0.32 ± 0.21	0.27 ± 0.26	0.21 ± 0.21	0.51 ± 0.11	10.61 ± 0.40	$2.96^{+0.02}_{-0.02}$	2.91 ± 0.25	–
2.2	104.65203	–55.950014	24.59 ± 0.06	0.56 ± 0.12	0.24 ± 0.09	0.21 ± 0.08	0.49 ± 0.05	14.18 ± 0.94	$3.09^{+0.73}_{-0.29}$	–	–
2.3	104.63801	–55.956311	26.35 ± 0.07	0.45 ± 0.16	0.44 ± 0.13	0.25 ± 0.10	0.57 ± 0.08	4.79 ± 0.21	$2.74^{+0.10}_{-0.02}$	–	–
3.1	104.65770	–55.948271	24.74 ± 0.05	0.61 ± 0.18	−0.01 ± 0.07	−0.09 ± 0.05	0.23 ± 0.02	9.37 ± 0.54	$4.16^{+0.22}_{-0.25}$	4.06 ± 1.23	–
3.2	104.65118	–55.950472	26.74 ± 0.08	0.95 ± 0.32	−0.22 ± 0.17	−0.26 ± 0.15	0.38 ± 0.12	4.73 ± 0.14	$4.32^{+0.28}_{-0.14}$	–	–
3.3	104.63565	–55.957061	>28.50	>1.51	−0.34 ± 0.07	−0.05 ± 0.27	0.53 ± 0.24	4.94 ± 0.22	$4.53^{+0.42}_{-0.55}$	–	–
4.1	104.64423	–55.949050	27.58 ± 0.38	0.21 ± 0.12	0.57 ± 0.04	−0.29 ± 0.04	−0.08 ± 0.05	22.96 ± 2.11	$2.03^{+1.1}_{-0.42}$	2.00 ± 0.12	–
4.2	104.64251	–55.950576	26.97 ± 0.28	0.28 ± 0.14	0.36 ± 0.07	−0.33 ± 0.05	−0.20 ± 0.04	20.04 ± 1.71	$0.17^{+2.28}_{-0.12}$	–	–
4.3*	104.65166	–55.944823	–	–	–	–	–	–	–	–	–
5.1	104.64961	–55.947382	27.44 ± 0.23	1.14 ± 0.21	−0.72 ± 0.19	−0.06 ± 0.17	0.26 ± 0.35	4.70 ± 0.20	$2.10^{+0.38}_{-0.21}$	2.54 ± 0.34	–
5.2	104.64928	–55.947412	27.56 ± 0.45	0.90 ± 0.18	−0.31 ± 0.12	−0.40 ± 0.10	0.21 ± 0.26	4.75 ± 0.20	$2.00^{+0.53}_{-0.18}$	–	–
5.3*	104.63731	–55.953223	–	–	–	–	–	–	–	–	
D.2[c]	104.63981	–55.947308	26.56 ± 0.20	−0.19 ± 0.08	0.02 ± 0.06	0.41 ± 0.04	0.27 ± 0.01	49.83 ± 10.34	$2.34^{+0.24}_{-0.45}$	–	–
D.1	104.63943	–55.947552	26.79 ± 0.24	−0.31 ± 0.14	−0.13 ± 0.16	0.80 ± 0.10	0.36 ± 0.02	50.19 ± 5.42	$2.56^{+0.74}_{-0.38}$	3.23 ± 0.42	–
D.3	104.64623	–55.944115	25.52 ± 0.22	−0.03 ± 0.07	0.17 ± 0.06	0.57 ± 0.03	0.32 ± 0.01	49.96 ± 3.23	$2.13^{+0.85}_{-0.89}$	–	–

Notes. The systems and their properties, along with references to the papers reporting their redshifts, are given in Sect. 3. Images marked * are not detected, thus their positions are just predictions from lens model. We do not report photometry on system K since it is smm galaxy, invisible in ACS/HST. [(a)] Redshift estimation inferred from the mass model when all spectroscopically confirmed multiply-imaged systems have been included in the optimization. [(b)] System Fa and Fb are most probably gravitationally bounded. [(c)] System D is not included in the model optimization, it is a multiply-imaged candidate. Numbers (.1, .2 , etc.) denote the different images of each set of multiple images. Each multiple image is presented in Fig. 5, except system K that is invisible in optical and system D that has not been included in the model optimization is presented in Fig. 7.

dark matter distribution. Because of this offset, including the gas mass as a separate component is important for accurate modeling of the total mass distribution. Therefore, we have included the intra-cluster gas (without optimization of this component) in our total mass model of the Bullet cluster (see Sect. 4.3) using the X-rays measurements performed by Ota & Mitsuda (2004), Markevitch et al. (2002).

Using the observational constraints (namely multiply image positions and photometric redshifts given in Tables 4 and 5) we have optimized the parameters of the mass components: the DM clumps, the BCGs and the individual galaxies (see Table 6). As a starting point, we have used a set of initial parameters (centroid, ellipticity and position angle) based on the visible component (Limousin et al. 2008), that were then iteratively optimized.

For each image, marginalising over the photometric redshift (if no spectroscopic redshift was known) we find its root-mean-square (rms) value for its position in the image plane, given by $\mathrm{rms} = \sqrt{\frac{1}{n}\sum_{j=1}^{n}(X^{j}_{\rm obs} - X^{j}_{\rm model})^2}$, where n is the number of images for the system, $X_{\rm model}$ is the predicted by model position in the image plane and $X_{\rm obs}$ the observed position in the image plane (see Table 7). The overall rms is defined by summing and averaging over all the images for all the systems. A detailed overview of the LENSTOOL software and discussion of parameters uncertainty can be found in Jullo et al. (2007). Thanks to the parallelized version of LENSTOOL the optimization could be efficiently performed in the image plane similarly as done in Limousin et al. (2012).

4.2. Scaling relation of elliptical cluster members

We lack sufficient sensitivity to constrain the detailed mass profile for individual cluster galaxies. Thus, in general, cluster modeling uses Faber-Jakson scaling relation (FJR, Faber & Jackson 1976) to scale the galaxy members. It assumes that all galaxies in the cluster have the same M/L ratio (Natarajan & Kneib 1997; Natarajan et al. 1998; Limousin et al. 2007b, 2005; Oguri 2010; Kneib et al. 2003; Richard et al. 2009; Jullo et al. 2010).

Table 5. Multiply-imaged systems used to constrain the model, with their centroid position, brightness, colors, linear magnification and predicted or spectroscopically measured redshifts.

System	RA (deg)	Dec (deg)	*F606W*	*F435W – F606W*	*F606W – F814W*	*F435W – F814W*	μ	$z_{\rm phot}$	$z_{\rm m}^{a}$	$z_{\rm spec}$
Sub clump										
H.1	104.56305	–55.939755	26.59 ± 0.08	0.65 ± 0.11	−0.21 ± 0.07	0.43 ± 0.12	6.48 ± 0.67	$3.3^{+0.2}_{-1.2}$	–	2.99
H.2	104.56145	–55.942423	26.78 ± 0.08	0.78 ± 0.14	−0.40 ± 0.09	0.36 ± 0.16	9.62 ± 0.87	$3.3^{+0.2}_{-0.7}$	–	–
H.3	104.56202	–55.947717	26.57 ± 0.12	1.00 ± 0.15	−0.29 ± 0.06	0.29 ± 0.14	11.74 ± 1.53	$2.7^{+0.9}_{-1.3}$	–	–
I.1n	104.56478	–55.938146	26.36 ± 0.14	0.47 ± 0.11	0.17 ± 0.07	0.64 ± 0.11	5.31 ± 0.50	$2.4^{+0.9}_{-1.4}$	–	–
I.2	104.56155	–55.944252	25.55 ± 0.07	0.50 ± 0.07	0.08 ± 0.04	0.59 ± 0.07	20.25 ± 3.38	$2.6^{+0.7}_{-1.5}$	3.24 ± 0.13	–
I.3	104.56192	–55.946101	25.60 ± 0.05	0.49 ± 0.06	0.03 ± 0.04	0.52 ± 0.06	15.91 ± 1.53	$2.6^{+0.7}_{-1.5}$	–	–
J.1	104.57038	–55.944036	26.81 ± 0.13	−0.11 ± 0.08	−0.47 ± 0.09	−0.58 ± 0.10	24.49 ± 4.01	$1.6^{+1.2}_{-0.6}$	2.02 ± 0.25	–
J.2	104.56917	–55.946003	27.03 ± 0.12	−0.32 ± 0.10	−0.19 ± 0.10	−0.50 ± 0.11	19.33 ± 1.99	$1.0^{+1.8}_{-0.0}$	–	–
J.3	104.56993	–55.938772	27.99 ± 0.55	−0.17 ± 0.21	−0.37 ± 0.16	−0.20 ± 0.18	5.39 ± 0.48	$0.9^{+2.3}_{-0.9}$	–	–
G.1	104.56580	–55.939857	25.31 ± 0.05	>1.85	0.40 ± 0.05	>2.25	11.60 ± 1.56	$3.3^{+1.5}_{-2.3}$	0.73 ± 0.09	–
G.2	104.56424	–55.941963	25.27 ± 0.06	>1.73	0.57 ± 0.06	>2.16	13.46 ± 1.04	$2.5^{+1.9}_{-0.8}$	–	–
G.3n*	104.56471	–55.947724	–	–	–	–	–	–		
6.1	104.56406	–55.945386	26.05 ± 0.08	−0.14 ± 0.09	0.25 ± 0.07	0.11 ± 0.08	40.90 ± 4.88	$0.9^{+1.1}_{-0.6}$	2.51 ± 0.12	–
6.2	104.56384	–55.944904	26.17 ± 0.11	−0.08 ± 0.09	0.15 ± 0.08	0.07 ± 0.09	31.30 ± 5.68	$0.8^{+1.9}_{-0.8}$	–	–
6.3*	104.56627	–55.938208	> 28.45	–	–	–	4.86 ± 0.43	–	–	
7.1^{b}	104.56084	–55.946952	26.89 ± 0.15	0.07 ± 0.35	−0.36 ± 0.45	−0.29 ± 0.23	22.71 ± 3.39	$1.4^{+1.9}_{-0.8}$	3.00 ± 0.19	–
7.2	104.56054	–55.942898	26.54 ± 0.12	0.15 ± 0.22	0.03 ± 0.32	0.18 ± 0.13	16.79 ± 1.90	$2.2^{+1.5}_{-1.5}$	–	–
7.3	104.56230	–55.939588	26.89 ± 0.13	0.03 ± 0.34	0.25 ± 0.29	0.28 ± 0.38	10.94 ± 0.78	$0.5^{+3.0}_{-0.4}$	–	–

Notes. The systems and their properties, along with references to the papers reporting their redshifts, are given in Sect. 3. Images marked * are not detected, thus their positions are just predictions from lens model. [(a)] Redshift estimation inferred from the mass model when all spectroscopically confirmed multiply-imaged systems have been included in the optimization. [(b)] System 7 is not included in the model optimization, it is multiply-imaged candidate. Numbers (.1, .2 , etc.) denote the different images of each set of multiple images, each presented in Fig. 6, except system 7 that has not been included in the model optimization.

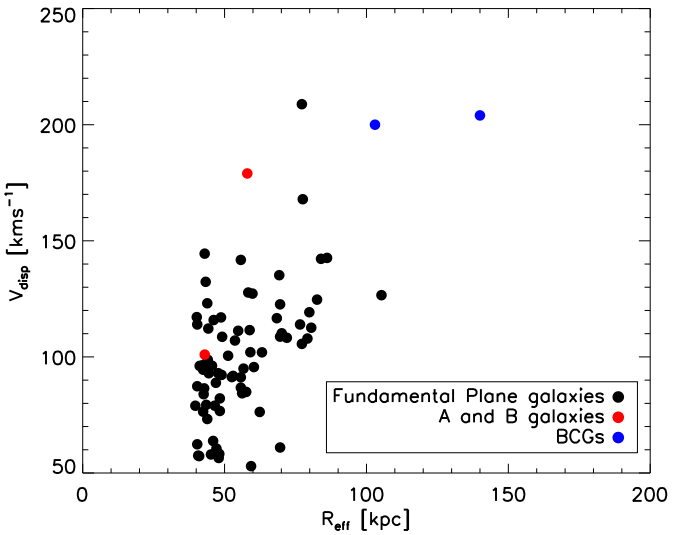

Fig. 8. Galaxy members identified using color-magnitude cut and comparison of the properties with separately modeled galaxies A and B (red) and BCGs (blue).

FJR is however, an empirical relation with a quite large scatter. For example, Nigoche-Netro et al. (2010) by analyzing the FJR showed that its parameters depend on the magnitude range.

In fact FJR is a projection of the fundamental plane (FP) relation. The fundamental plane (Djorgovski & Davis 1987) is a tight correlation for elliptical galaxies between $R_{\rm eff}$ the effective radius, σ the central velocity dispersion, and $\langle I \rangle_{\rm e}$ the mean effective surface brightness, and can read:

$$\log R_{\rm eff} = a \log \sigma_{\rm FP} + b \log \langle I \rangle_{\rm e} + c, \quad (3)$$

where a, b, c are free parameters of this relation.

It is understood that the FP is a consequence of virial theorem of the dynamical equilibrium condition of elliptical galaxies. Although FP is tilted relative to the simple virial theorem prediction (Busarello et al. 1997), FP has been successfully used in various studies describing elliptical galaxies and in strong lens mass modeling by e.g., D'Aloisio & Natarajan (2011), Jullo et al. (2007), Halkola et al. (2006), Natarajan & Kneib (1997). The same physical motivation that led to the FJ, FP relations apply also to galaxies within a cluster: more luminous galaxies are more massive and rotate faster. Of course, in such a disturbed cluster like 1E 0657-56, the scatter of the relations might be larger than in the field, nevertheless the physical motivation remains. Therefore, in this paper we have applied FP to scale early-type cluster members.

For the FP scaling, we employ the parameters derived by Bernardi et al. (2003) for r-band, $a = 1.49, b = -0.75, c = 8.778$, as their galaxy sample has similar properties to the galaxy members in the Bullet cluster. Bernardi et al. (2003) have used a magnitude-limited sample of nearly 9000 early-type galaxies in the redshift range $0.01 < z < 0.3$ that was selected from the Sloan Digital Sky Survey (SDSS) using morphological and spectral criteria. They concluded that FP parameters depend only little on the sample redshifts at $0.01 < z < 0.3$ and likewise they found only slight dependence on environment. Still, we apply the redshift evolution that was found by Bernardi et al. (2003), who

Table 6. Modeled parameters of the three different mass model approaches. *Top* – model with Faber-Jackson scaling relation, *middle* – model with fundamental plane scaling relation and *bottom* – our final model with explicitly included X-rays gas mass plus fundamental plane scaling relations.

System	$\Delta\alpha$ ($''$)	$\Delta\delta$ ($''$)	ϵ	θ^a	$r_{\rm core}$ (kpc)	$r_{\rm cut}$ ($''$)	σ_0 (km s^{-1})
FJ log(Evidence) = –35.1			$\mathrm{rms_{FJ}} = 0.197''$				
DM 1	8.3 ± 0.3	−2.5 ± 0.8	0.64 ± 0.05	72.0 ± 2.1	117.4 ± 5.9	[1000.0]	884.2 ± 31.9
DM 2	24.2 ± 1.0	28.3 ± 1.2	0.13 ± 0.11	56.6 ± 1.0	127.3 ± 17.1	[1000.0]	840.2 ± 37.5
DM 3	185.9 ± 0.3	50.1 ± 0.1	0.46 ± 0.05	5.2 ± 0.5	47.3 ± 0.9	[1000.0]	795.7 ± 18.9
BCG 1	[0.00]	[0.00]	[0.26]	[43.5]	[0.3]	150.0 ± 2.1	255.9 ± 39.3
BCG 2	[24.05]	[29.13]	[0.20]	[37.4]	[0.2]	112.2 ± 1.8	201.6 ± 2.4
Gal A	[51.94]	[48.93]	[0.13]	[9.9]	[0.1]	60.0 ± 0.9	199.3 ± 3.9
Gal B	[5.23]	[23.01]	[0.10]	[−49.0]	[0.1]	53.3 ± 1.3	105.1 ± 1.6
$\sigma^\star_{\rm FJ}$	...	...	...	...	[0.1]	48.6 ± 8.5	119.2 ± 5.1
FP log(Evidence) = –34.0			$\mathrm{rms_{FP}} = 0.160''$				
DM 1	8.2 ± 0.3	−2.3 ± 0.7	0.56 ± 0.07	72.4 ± 2.6	125.8 ± 7.0	[1000.0]	938.1 ± 39.0
DM 2	24.8 ± 0.8	27.9 ± 1.0	0.23 ± 0.09	55.4 ± 1.1	133.4 ± 7.6	[1000.0]	847.0 ± 42.0
DM 3	186.0 ± 0.4	50.1 ± 0.1	0.44 ± 0.04	4.8 ± 0.5	50.0 ± 3.0	[1000.0]	815.2 ± 16.8
BCG 1	[0.00]	[0.00]	[0.26]	[43.5]	[0.3]	50.5 ± 12.3	201.8 ± 32.0
BCG 2	[24.05]	[29.13]	[0.20]	[37.4]	[0.2]	48.8 ± 5.8	212.7 ± 7.2
Gal A	[51.94]	[48.93]	[0.13]	[9.9]	[0.1]	48.1 ± 10.1	230.5 ± 4.9
Gal B	[5.23]	[23.01]	[0.10]	[−49.0]	[0.1]	48.5 ± 2.2	117.2 ± 13.1
$S_{\rm FP}$	...	...	...	...	[0.1]	71.1 ± 5.1	1.16 ± 0.14[b]
FP log(Evidence) = –31.7			$\mathrm{rms_{FP+X}} = 0.147''$				
DM 1	9.6 ± 0.4	−1.6 ± 1.6	0.41 ± 0.06	81.7 ± 3.8	131.2 ± 12.3	[1000.0]	918.6 ± 49.6
DM 2	21.6 ± 1.2	25.6 ± 2.1	0.43 ± 0.07	64.5 ± 1.8	108.5 ± 12.5	[1000.0]	733.0 ± 54.9
DM 3	185.6 ± 0.3	50.1 ± 0.1	0.30 ± 0.02	3.5 ± 0.7	58.9 ± 1.2	[1000.0]	862.2 ± 7.0
BCG 1	[0.00]	[0.00]	[0.26]	[43.5]	[0.3]	49.2 ± 5.8	302.3 ± 10.5
BCG 2	[24.05]	[29.13]	[0.20]	[37.4]	[0.2]	50.3 ± 7.2	215.5 ± 7.6
Gal A	[51.94]	[48.93]	[0.13]	[9.9]	[0.1]	49.5 ± 6.8	224.4 ± 5.8
Gal B	[5.23]	[23.01]	[0.10]	[−49.0]	[0.1]	51.4 ± 7.0	117.5 ± 13.5
$S_{\rm FP}$	...	...	...	...	[0.1]	93.1 ± 59.3	1.19 ± 0.76[b]

Notes. Values quoted within brackets were kept fixed in the optimization. The error bars correspond to 68% confidence levels. The location and the ellipticity of the matter clumps associated with the cluster galaxies were kept fixed according to the light distribution. The ellipticity ϵ is the one of the mass distribution, expressed as a^2-b^2/a^2+b^2. The center is defined at $\alpha = 104.6588589$ $\delta = -55.9571863$ in J2000 coordinates corresponding to the center of the first BCG. [(a)] Position angle of the potential distribution expressed in degree, 90° relative to PA. It corresponds to the direction of the semi-minor axis of the isopotential counted from the horizontal axis, counterclockwise. [(b)] This is fundamental plane parameter described in Eq. (4), it is a factor S that translates $\sigma_{\rm FP}$ into $\sigma_{\rm dPIE}$.

showed that, on average, the higher redshift galaxies are brighter, with the brightening scaling approximately as $\Delta\mu_0 \approx 2z$. This directly translates to FP scaling parameters we use, the evolved parameters are now: $a = 1.49, b = -0.75, c = 8.946$.

We have derived $\sigma_{\rm FP}$ for each cluster member (see Eq. (3)) using the two observables $\langle I\rangle_{\rm e}$ and $R_{\rm eff}$. To get a reliable estimate of the effective radius used in the fundamental plane scaling relation, we have performed a fit of the light distribution for cluster members selected through the red sequence. We used the software GALAPAGOS (Barden et al. 2012) on the ACS/*F606W Hubble* image to automatically create input parameter files for GALFIT (Peng et al. 2011) on each galaxy. The light distribution is fit by a Sersic profile where we adjusted the total flux, effective radius, ellipticity and position angle, while fixing central position and the Sersic index to $n = 4$ to prevent degeneracies with the effective radius.

Parameters $\sigma_{\rm FP}$ and $\sigma_{\rm dPIE}$ are indeed conceptually different quantities: $\sigma_{\rm FP}$ is the random motion of the stars and $\sigma_{\rm dPIE}$ is normalization of the mass profile, they also differ by the radius over which they are defined, $r_{\rm cut} \gg R_{\rm eff}$ (the galaxy mass component is including both stellar mass and dark matter mass). Even though $\sigma_{\rm dPIE}$ is a fiducial velocity dispersion, we wish to relate it to the measured velocity dispersion $\sigma_{\rm FP}$ of galaxies, assuming that their profile is described by a dPIE. Therefore, we have scaled the $\sigma_{\rm FP}$ by the factor S that is optimized in the modeling process.

$$\sigma_0 = S_{\rm FP}\sigma_{\rm FP}, \tag{4}$$

$$r_{\rm cut} = r^*_{\rm cut}\left(\frac{L}{L^*}\right)^{1/2}, \tag{5}$$

$$r_{\rm core} = r^*_{\rm core}\left(\frac{L}{L^*}\right)^{1/2}, \tag{6}$$

where $L^\star$, $r^\star_{\rm core}$ and $r^\star_{\rm cut}$ are, the luminosity, core radius and cut radius, the dPIE parameters of a typical cluster galaxy (Limousin et al. 2007b).

Table 7. Goodness of fit of the three different Bullet cluster models.

System	(1) rms_{FJ} ($''$)	(2) rms_{FP} ($''$)	(3) rms_{Xrays} ($''$)
A.1	0.145	0.193	0.196
A.2	0.026	0.065	0.112
A.3	0.119	0.129	0.125
Fa.1	0.205	0.077	0.032
Fa.2	0.274	0.078	0.110
Fa.3	0.128	0.123	0.130
Fb.1	0.183	0.077	0.110
Fb.2	0.253	0.078	0.032
Fb.3	0.102	0.123	0.160
E.1	0.247	0.101	0.030
E.2	0.254	0.101	0.030
E.3	0.290	0.101	0.030
K.1	0.300	0.230	0.226
K.2	0.132	0.149	0.125
K.3	0.215	0.096	0.104
1.1	0.252	0.124	0.144
1.2	0.551	0.124	0.144
2.1	0.150	0.091	0.070
2.2	0.085	0.071	0.046
2.3	0.164	0.021	0.026
3.1	0.046	0.245	0.194
3.2	0.046	0.193	0.134
3.3	0.046	0.065	0.318
4.1	0.172	0.079	0.147
4.2	0.075	0.079	0.147
5.1	0.096	0.028	0.027
5.2	0.056	0.028	0.027
H.1	0.237	0.248	0.233
H.2	0.209	0.375	0.302
H.3	0.076	0.128	0.096
I.1	0.367	0.249	0.132
I.2	0.356	0.049	0.093
I.3	0.082	0.284	0.182
J.1	0.084	0.201	0.195
J.2	0.084	0.296	0.201
J.3	0.145	0.434	0.357
G.1	0.345	0.036	0.046
G.2	0.045	0.036	0.046
6.1	0.054	0.038	0.045
6.2	0.078	0.038	0.045
6.3	0.752	0.038	0.045
Total rms	0.197	0.160	0.147

Notes. [(1)] Faber Jackson relation; [(2)] fundamental plane; and [(3)] X-rays with fundamental plane. The rms represents the difference between measured position of the images and the position predicted by the model.

4.3. X-rays

Gas in galaxy clusters represent ∼10−15% of the total mass, which can be fairly easily measured with X-rays (e.g., David et al. 1993; Neumann & Arnaud 2001; Vikhlinin et al. 2006; LaRoque et al. 2006). However, gas is generally not included explicitly in cluster lens modeling (with a few exceptions, e.g., Bradač et al. 2008). This is partly due to the fact that in relaxed clusters gas is centered in the same region as dark matter hence it can not be disentangled from the dark matter component.

However, in the Bullet cluster there is a significant offset between the gas and dark matter distribution. Thus, including the gas mass as a separate component of the mass model is essential for realistic modeling the total mass distribution of the bullet cluster. Moreover, due to the offset, gas distribution in this cluster has been well studied (Ota & Mitsuda 2004; Markevitch et al. 2002).

X-ray emission in the intra-cluster gas is dominated by thermal bremsstrahlung, and it is proportional to the line-of-sight integral of the square of the electron density. Due to lack of strongly lensed images in vicinity of the gas density centers we expect that the gas mass in the Bullet cluster provides only an external shear to the strong lens model. However, to compare the effect of the gas mass distribution on the results, we create two fiducial models for the spatial distribution of the total (main+sub) intra-cluster gas mass. centered For our fiducial model X1, we take the spatial distribution of the total (main+sub) intra-cluster gas as a spherical model derived from ROSAT HRI measurements resolution of Ota & Mitsuda (2004), $\beta = 1.04$, $\theta_c = 112.5''$, $n_{e0} = 7.2 \times 10^{-3}$ cm^{-3}. And we obtain a surface gas mass map by projection of the β-model gas density profile:

$$M_{gas,2D}(r) = 2\,\rho_{gas,0}\,r_c\,g(\beta)\left(1+\frac{r^2}{r_c^2}\right)^{-3\beta/2+1/2}, \quad (7)$$

with $g(\beta) = 1/2\,\Gamma(1/2)\Gamma(3\beta/2{-}1/2)/\Gamma(3\beta/2)$, $\rho_{gas,0}$ the gas mass density at the center and r_c the core radius.

In the second fiducial model X2, we assume as an approximation that X-ray emission is proportional to the square of the mass density. We assume that this is tenable in the central region. We take a square root of the smoothed (convolution by a Gaussian of $\sigma = 2$ pixels) X-ray count map from the 500 ks *Chandra* ACIS-I observations (Markevitch 2006) and we normalize it.

The normalisation factor is computed by matching the gas mass to the one obtained by the β model determined from above mentioned ROSAT HRI measurements of X-ray gas mass. The total mass within $30''$ radius of this projected model is $2.1 \times 10^{13}\ M_\odot$.

We have included the X-rays gas mass maps into our lens model using the grid technique implemented in LENSTOOL (Jullo & Kneib 2009), and compared the results for the 2 different fiducial models. The code iteratively splits the $200'' \times 200''$ mass map into equilateral triangles as a function of a mass threshold. At each node of this multi-scale grid a mass profile is described by a dPIE potential whose core radius is equal to the local grid resolution and a cut-off radius equals to three times the core radius. We force the algorithm to stop after four levels of splitting and as a result we have a grid cell containing ∼50 dPIE potentials describing the smooth gas distribution.

4.4. Results

The optimized mass model and critical lines predicted by the model at $z = 3.24$ are presented in Fig. 9. We have used the two different common scaling relation and also included the gas measured using X-rays. For our best models we find $rms_{FJ} = 0.197''$ for Faber Jackson relation, $rms_{FP} = 0.160''$ for fundamental

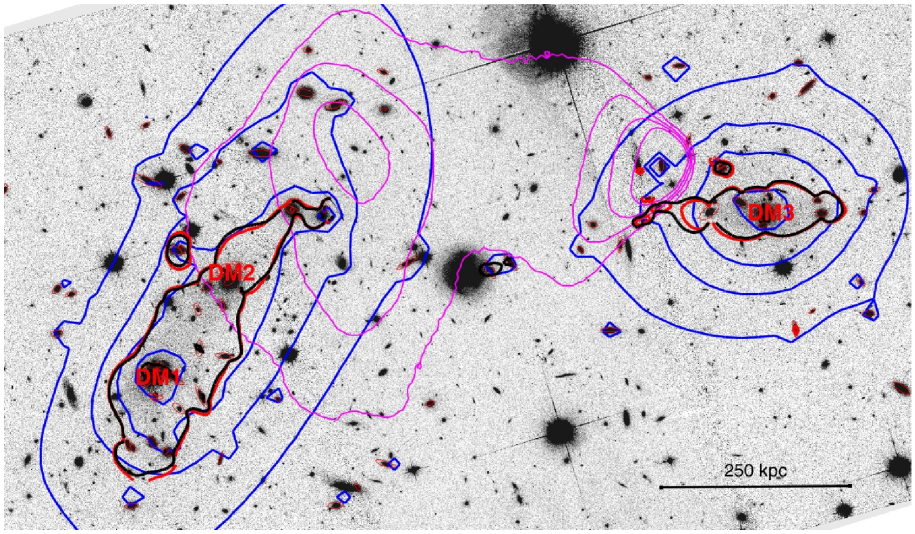

Fig. 9. *F606W*-band image of the Bullet cluster. The size of the field of view is 150″ × 250″. The blue contours show the projected mass density. The red line represents a critical line calculated using Faber-Jackson scaling relation to all cluster members while black line represents the result from use of the scaling relation, fundamental plane. The magenta lines represent the contours of the *Chandra* X-rays brightness map.

plane and $\mathrm{rms}_{X1} = 0.147''$ and $\mathrm{rms}_{X2} = 0.149''$ for fundamental plane + X-rays (X1 and X2) (see Fig. 9 and Table 6).

Clearly, the influence of scaling relation on overall cluster mass model is minor, the fit of the model to the data seems to be very similar for both scalings, however it might be important for future detailed studies of galaxy clusters, for example, cluster lensing cosmography (Jullo et al. 2010; D'Aloisio & Natarajan 2011).

However, the rms of the model with explicitly included X-rays gas is better than without gas. The different gas mass distribution, derived with two different methods seems not to have a significant effect on the model fitting ($\mathrm{RSM}_{X1} = 0.147''$ vs. $\mathrm{RSM}_{X2} = 0.149''$). This is most probably due to the flexibility of the DM model. Apparently, the influence of gas mass is small enough that the model can compensate it by changing slightly the parameters of DM halos (position, ellipticity and size) without losing precision of the multiple images position reconstruction. Nevertheless, including well measured gas mass is clearly a logical choice and does improve the rms of the model. This is especially important in case of the Bullet cluster where DM and gas are spatially separated.

The Bayesian evidences (see, Jullo et al. 2007) reported in Table 6 correctly summarize these observations. According to Jeffreys (1961), the difference between two models is substantial if $1 < \Delta\ln(E) < 2.5$, strong if $2.5 < \Delta\ln(E) < 5$ and decisive if $\Delta\ln(E) > 5$. Following this criterion, there is a strong evidence that model with X-ray is better than those without.

In Fig. 9 we show the *F606W*-band image of the Bullet cluster along with the contours generated from the projected mass map inferred from the best-fit model. This mass map is found to be in very good agreement with the light distribution. We find that the mass distribution of the Bullet cluster consists of three dark matter clumps, the main clump of the Bullet cluster is bimodal, which is in agreement with previous models of the Bullet cluster. We find that DM1 and DM2 have high ellipticity and DM1 is comparable in mass to DM2 (see Table 6).

Furthermore, the galaxies and dark matter distributions share comparable centroid position, orientation and ellipticity. The agreement is a proof of the collisionless nature of dark matter, as suggested from the Bullet cluster by Clowe et al. (2006). By integrating our two dimensional mass map, we get the total mass profile shown in Fig. 11. In Fig. 9 we compare also critical lines position derived by FP relation by plotting the critical lines of the two models corresponding to $z = 3.24$, showing good agreement of these models.

We also compare the mass associated with the individual galaxies (M_{galax}) together with the 3 BCGs to the total mass (M_{tot}) as a function of radius (see Fig. 12). Inside radius $R <$ 250 kpc, we find $M_{\mathrm{tot}} = 2.5 \pm 0.1 \times 10^{14}\ M_{\odot}$, we find also that the contribution of the galaxy halos to the total mass is 11 ± 5% at 250 kpc. As shown in Fig. 12 this fraction increases towards the center of the cluster, similar results were also observed in by Kneib et al. (2003), Limousin et al. (2007b).

As compare to previous Bullet cluster studies the main and sub clump masses estimated in this work are respectively (11 ± 4)% and (27 ± 12)% smaller to those predicted by Bradač et al. (2006). Although the difference in estimated mass is only marginally significant, the changes in the model lead to substantially different predictions for the magnification of sources near the critical lines. Indeed, to measure an impact of our strong lensing mass map, we have measured the magnification of the dropout high-z galaxies found and analyzed by Hall et al. (2012). We find that average magnification of those dropouts estimated by our mass model is 43% smaller than predicated by Hall et al. (2012), see Fig. 10. This is expected since high redshift critical lines of our mass model lie closer to the center of the cluster than those of Bradač et al. (2009), this is specially true for southern part of the cluster where all the droupouts are located (see Fig. 1 and Table 1 at Hall et al. 2012).

We note that, our mass model along with all methods of strong-lensing mass reconstruction have degenerate and non orthogonal parameters. There are numerous publications detailing this strong lensing modeling degeneracies (see, Jullo et al. 2007; Meneghetti et al. 2007, etc.). In summary, parameters of all lens models are clearly dependent on each other and they often compensate in order to produce a constant enclosed mass at the images location, causing, for example, that the enclosed mass in the Einstein radius decreases with the model ellipticity. The most relevant findings for this work was observed by Jullo et al. (2007) that the dPIE cut-off radius (but also the Sersic effective radius and the NFW scale radius) is one of the less constrained parameter by strong lensing, as it lies beyond the outermost

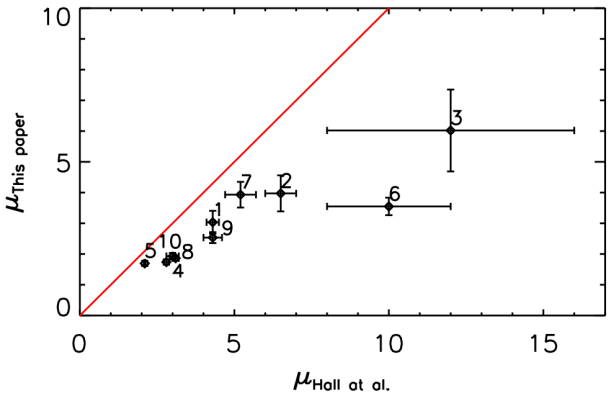

Fig. 10. Magnification measurements of the dropout high-z galaxies found and analyzed by Hall et al. (2012). We find that average magnification of those dropouts estimated by our mass model is 43% smaller than predicated by Hall et al. (2012). This is expected since high redshift critical lines of our mass model lie closer to the center of the cluster than those of Bradač et al. (2009).

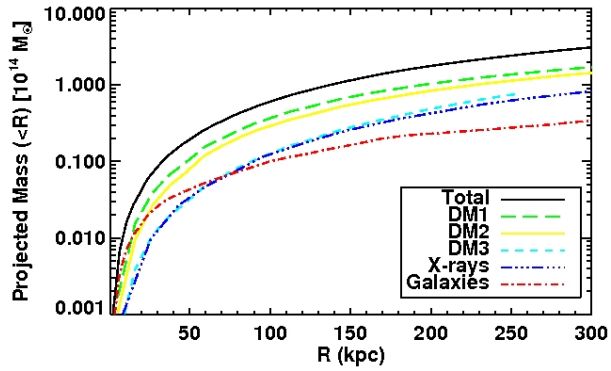

Fig. 11. Total projected mass as a function of aperture radius centered at BCG1 (for the simplicity of the comparison with results of Bradač et al. 2006) for different model components. The two large scale clumps, DM1 and DM2, contribute a similar amount to the mass, the X-rays gas mass measured by (Markevitch et al. 2004) is ∼9 ± 3% to the total mass at 250 kpc radius. The galaxies (including the BCG) contribute 11 ± 5% within a 250 kpc radial aperture.

multiply imaged system. Moreoever, there is a severe degeneracy is between galaxy-scale subhalos and the cluster-scale halo, especially when no multiple images appear in the cluster. centre. However, they also found that the best constraints parameters were obtained in lensing configurations combining radial and tangential multiple image configurations, as it is the case of Bullet cluster. Additionally, as shown by Natarajan et al. (1998) weak and strong lensing provide tighter parameter constraints. Nevertheless, as it was mention before, combining the our strong lens model with weak lensing is out of scope of this paper and will be subject of in our next work.

Along with these degeneracies our mass model can have possible systematic error due to misidentification of multiple images and inaccuracy of their photometric redshift. All this can potentially make a precise model fairly inaccurate. To minimize the possibility of this source of error we have thoroughly reviewed each strongly lensed candidate proposed by searches by checking the morphology and color agreements. Though only spectroscopical data would give ultimate confirmation.

We estimated the redshifts of the new candidate systems using the model predictions. The estimated redshifts are reported in

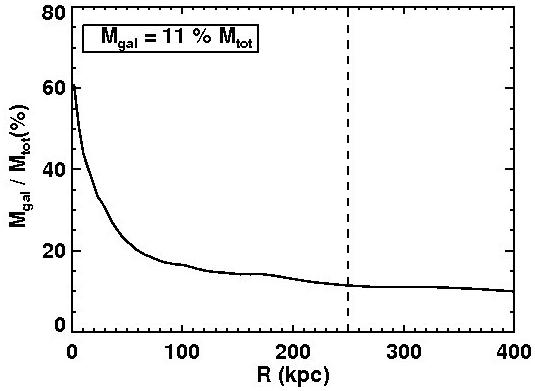

Fig. 12. Contribution of the galaxy component to the total mass as a function of radius (centered on the BCG 1). The vertical dotted line shows the location of the 250 kpc radius where $M_{\rm gal} = 11 \pm 5\% M_{\rm tot}$.

Tables 4 and 5. A summary of the best-fit values inferred through the strong lensing optimization are reported in Table 6.

Finally, we have looked at the difference between measured σ and $R_{\rm eff}$ of BCGs and A,B galaxy and inferred properties (σ and $R_{\rm eff}$) of the rest cluster members. We found that $\langle\sigma\rangle = 100 \pm 28$ km s^{-1} and $\langle R_{\rm eff}\rangle = 56 \pm 14$ kpc for galaxy member, and also we find that out of the 82 elliptical galaxies in the catalog 35 are with $\sigma < 100$ km s^{-1}. One of the two galaxies that has been separately modeled (galaxy A) have the two properties within the average galaxy member distribution $\sigma = 101 \pm 5$ km s^{-1} and $R_{\rm eff} = 43 \pm 2$ kpc, while the velocity dispersion of the galaxy B is bigger then average galaxy member by 79 ± 37% (see Fig. 8).

5. Conclusions

Due to its rare characteristic (spatial separation of the X-ray gas and the rest of the matter), the Bullet cluster is an object of great interest for fundamental physics. The detailed study of its total mass distribution not only brings answers about existence and nature of dark matter but also provides an exceptionally strong gravitational telescope.

In this work we have reconstructed a mass map of the galaxy cluster 1E 0657-56 using strong lensing constraints and X-rays data. Using deep, high-resolution optical data we have revised the previously known multiply-imaged systems and identify new ones. As a result our model is based on 14 multiply-imaged systems with 3 spectroscopic redshifts. The model was sampled and optimized in the image plane by a Bayesian Monte Carlo Markov chain implemented in the publicly available software LENSTOOL. Our main conclusions are as follows:

1. Using the strong lensing mass reconstruction we derive a high-resolution mass map; we get a projected, enclosed mass $M_{\rm main}(R < 250\ {\rm kpc}) = 2.5 \pm 0.1 \times 10^{14}\ M_\odot$ and $M_{\rm sub}(R < 250\ {\rm kpc}) = 2.0 \pm 0.2 \times 10^{14}\ M_\odot$. The main and sub clump masses are respectively (11 ± 4)% and (27 ± 12)% smaller to those predicted by Bradač et al. (2006).
2. We have presented the implementation of the fundamental plane as a cluster members scaling relation and X-rays gas mass maps into the strong lensing mass modeling. We have shown that model with scaling scaling relation fundamental plane together with explicit inclusion of X-ray gas has the best ${\rm rms}_{\rm FP+X} = 0.147''$. The other two models have worse, yet similar precision. The mass model without explicit X-ray gas has ${\rm rms}_{\rm FP} = 0.160''$ and mass model without explicit X-ray gas and FJ as scaling relation has ${\rm rms}_{\rm FJ} = 0.197''$.

3. We have found, in agreement with previous models of 1E 0657-56 that the major mass component (cluster scale-DM halos) is in spatial agreement with the galaxies and not with the X-rays gas, which confirms the collisionless nature of dark matter. We detect the main and sub cluster DM peak being aligned with their BCGs, both clearly offset from the location of the X-ray gas in the system.

The high precision mass map we have presented is made available to the community and can be used to exploit 1E 0657-56 as a gravitational telescope, probing the high redshift universe (e.g., Bradač et al. 2009; Kneib et al. 2004).

Acknowledgements. D.P. acknowledges support from Agence Nationale de la Recherche bearing the reference ANR-09-BLAN-0234-01. J.P.K. and M.L. acknowledges support from CNRS. J.R. acknowledges support from the ERC starting grant CALENDS. J.P.K. acknowledge support from the ERC Advanced Grant project "Light on the Dark" (LIDA). The Dark Cosmology Centre is funded by the Danish National Research Foundation. Data presented herein were obtained as part of programs 11591, 11099, 10863, 10200 from the NASA/ESA *Hubble* Space Telescope. Also partially based on European Southern Observatory program 084.B-0523 (PI: Mei). A.M. gratefully acknowledges the hospitality of the Harvard-Smithsonian Center for Astrophysics and of the NASA's Goddard Space Flight Center and he acknowledges support from *Chandra* grants GO2-13160A, GO2-13102A, GO4-15115X and NASA grant NNX14AI29G.

References

Appenzeller, I., Fricke, K., Fürtig, W., et al. 1998, The Messenger, 94, 1
Barden, M., Häußler, B., Peng, C. Y., McIntosh, D. H., & Guo, Y. 2012, MNRAS, 422, 449
Barrena, R., Biviano, A., Ramella, M., Falco, E. E., & Seitz, S. 2002, A&A, 386, 816
Bekenstein, J. D. 2004, Phys. Rev. D, 70, 083509
Bernardi, M., Sheth, R. K., Annis, J., et al. 2003, AJ, 125, 1866
Bertin, E., & Arnouts, S. 1996, A&AS, 117, 393
Boyarsky, A., Ruchayskiy, O., & Markevitch, M. 2008, ApJ, 673, 752
Bradač, M., Clowe, D., Gonzalez, A. H., et al. 2006, ApJ, 652, 937
Bradač, M., Allen, S. W., Treu, T., et al. 2008, ApJ, 687, 959
Bradač, M., Treu, T., Applegate, D., et al. 2009, ApJ, 706, 1201
Busarello, G., Capaccioli, M., Capozziello, S., Longo, G., & Puddu, E. 1997, A&A, 320, 415
Clowe, D., Gonzalez, A., & Markevitch, M. 2004, ApJ, 604, 596
Clowe, D., Bradač, M., Gonzalez, A. H., et al. 2006, ApJ, 648, L109
D'Aloisio, A., & Natarajan, P. 2011, MNRAS, 411, 1628
David, L. P., Slyz, A., Jones, C., et al. 1993, ApJ, 412, 479
Djorgovski, S., & Davis, M. 1987, ApJ, 313, 59
Faber, S. M., & Jackson, R. E. 1976, ApJ, 204, 668
Gerhard, O., Kronawitter, A., Saglia, R. P., & Bender, R. 2001, AJ, 121, 1936
Gonzalez, A. H., Papovich, C., Bradač, M., & Jones, C. 2010, ApJ, 720, 245
Halkola, A., Seitz, S., & Pannella, M. 2006, MNRAS, 372, 1425
Hall, N., Bradač, M., Gonzalez, A. H., et al. 2012, ApJ, 745, 155
Jauzac, M., Richard, J., Jullo, E., et al. 2015, MNRAS, 452, 1437
Jeffreys, H. 1961, Theory of Probability (Oxford: Oxford Univ. Press)
Jullo, E., & Kneib, J.-P. 2009, MNRAS, 395, 1319
Jullo, E., Kneib, J., Limousin, M., et al. 2007, New J. Phys., 9, 447
Jullo, E., Natarajan, P., Kneib, J.-P., et al. 2010, Science, 329, 924
Kneib, J., Ellis, R. S., Smail, I., Couch, W. J., & Sharples, R. M. 1996, ApJ, 471, 643
Kneib, J., Hudelot, P., Ellis, R. S., et al. 2003, ApJ, 598, 804
Kneib, J.-P., Ellis, R. S., Santos, M. R., & Richard, J. 2004, ApJ, 607, 697
Koekemoer, A. M., Fruchter, A. S., Hook, R. N., & Hack, W. 2002, in The 2002 HST Calibration Workshop: Hubble after the Installation of the ACS and the NICMOS Cooling System, eds. S. Arribas, A. Koekemoer, & B. Whitmore, 337
Koopmans, L. V. E., Treu, T., Bolton, A. S., Burles, S., & Moustakas, L. A. 2006, ApJ, 649, 599
LaRoque, S. J., Bonamente, M., Carlstrom, J. E., et al. 2006, ApJ, 652, 917
Limousin, M., Kneib, J., & Natarajan, P. 2005, MNRAS, 356, 309
Limousin, M., Kneib, J. P., Bardeau, S., et al. 2007a, A&A, 461, 881
Limousin, M., Richard, J., Jullo, E., et al. 2007b, ApJ, 668, 643
Limousin, M., Richard, J., Kneib, J.-P., et al. 2008, A&A, 489, 23
Limousin, M., Ebeling, H., Richard, J., et al. 2012, A&A, 544, A71
Markevitch, M. 2006, in The X-ray Universe 2005, ESA SP 604, ed. A. Wilson, 723
Markevitch, M., Gonzalez, A. H., David, L., et al. 2002, ApJ, 567, L27
Markevitch, M., Gonzalez, A. H., Clowe, D., et al. 2004, ApJ, 606, 819
Mehlert, D., Seitz, S., Saglia, R. P., et al. 2001, A&A, 379, 96
Meneghetti, M., Bartelmann, M., Jenkins, A., & Frenk, C. 2007, MNRAS, 381, 171
Milgrom, M. 1983, ApJ, 270, 365
Natarajan, P., & Kneib, J.-P. 1997, MNRAS, 287, 833
Natarajan, P., Kneib, J., Smail, I., & Ellis, R. S. 1998, ApJ, 499, 600
Natarajan, P., Kneib, J.-P., Smail, I., et al. 2009, ApJ, 693, 970
Neumann, D. M., & Arnaud, M. 2001, A&A, 373, L33
Nigoche-Netro, A., Aguerri, J. A. L., Lagos, P., et al. 2010, A&A, 516, A96
Oguri, M. 2007, ApJ, 660, 1
Oguri, M. 2010, PASJ, 62, 1017
Ota, N., & Mitsuda, K. 2004, A&A, 428, 757
Peng, E. W., Ford, H. C., & Freeman, K. C. 2004, ApJ, 602, 705
Peng, C. Y., Ho, L. C., Impey, C. D., & Rix, H.-W. 2011, GALFIT: Detailed Structural Decomposition of Galaxy Images (Astrophysics Source Code Library)
Randall, S. W., Markevitch, M., Clowe, D., Gonzalez, A. H., & Bradač, M. 2008, ApJ, 679, 1173
Rex, M., Rawle, T. D., Egami, E., et al. 2010, A&A, 518, L13
Richard, J., Kneib, J., Jullo, E., et al. 2007, ApJ, 662, 781
Richard, J., Pei, L., Limousin, M., Jullo, E., & Kneib, J. P. 2009, A&A, 498, 37
Richard, J., Kneib, J.-P., Limousin, M., Edge, A., & Jullo, E. 2010a, MNRAS, 402, L44
Richard, J., Smith, G. P., Kneib, J.-P., et al. 2010b, MNRAS, 404, 325
Richard, J., Jauzac, M., Limousin, M., et al. 2014, MNRAS, 444, 268
Suyu, S. H., & Halkola, A. 2010, A&A, 524, A94
Tucker, W., Blanco, P., Rappoport, S., et al. 1998, ApJ, 496, L5
Vikhlinin, A., Kravtsov, A., Forman, W., et al. 2006, ApJ, 640, 691